Vehicular Communications 30 (2021) 100358

Contents lists available at ScienceDirect

Vehicular Communications

www.elsevier.com/locate/vehcom

Doppler-tolerant sequence design for positioning high-speed vehicles in millimeter-wave cellular systems

Mohammed Saquib Khan [a], Chang Hwan Park [b], Jingon Joung [a], Yong Soo Cho [a,*]

[a] Department of Electrical and Electronics Engineering, Chung-Ang University, Seoul 06974, South Korea
[b] LG Electronics, Seoul, 06772, South Korea

ARTICLE INFO

Article history:
Received 25 September 2020
Received in revised form 29 January 2021
Accepted 28 March 2021
Available online 1 April 2021

Keywords:
Doppler
High-speed vehicle
Millimeter-wave
Oscillatory pulse sequence
Positioning

ABSTRACT

Future fifth-generation (5G) New Radio (NR) services consider positioning an integral part of a system that provides high precision using millimeter-wave (mmWave) cellular networks. While the 5G standard for positioning is not fully defined yet, the positioning reference signal (PRS) used in long-term evolution (LTE) system is being considered. Since the conventional LTE PRS is designed for LTE systems below 6 GHz, it is more sensitive and inefficient for high-speed vehicle (HSV) experiencing a high Doppler effect in mmWave cellular systems. In this paper, a new sequence, called an oscillatory pulse sequence (OPS), is proposed for the positioning of HSVs in mmWave cellular systems. The ambiguity function (AF) and cross-ambiguity function of OPS are analyzed to examine its autocorrelation and cross-correlation properties in the existence of Doppler shift. The performance of the proposed OPS is compared with the performance of LTE PRS, Zadoff-Chu, and linear-frequency modulated waveforms with respect to correlation, time ambiguity, and Doppler tolerance. The analytic and simulation results show that the OPS provides an accurate timing (distance) estimation in the existence of a high Doppler shift, which is the ideal characteristic of the AF for positioning. The OPS is especially suitable for orthogonal frequency division multiplexing (OFDM) systems because it can be easily multiplexed with other signals in the frequency domain.

© 2021 The Author(s). Published by Elsevier Inc. This is an open access article under the CC BY-NC-ND license (http://creativecommons.org/licenses/by-nc-nd/4.0/).

1. Introduction

Future fifth-generation (5G) technologies will make spectrum bands above 24 GHz, known as millimeter-wave (mmWave) bands, available for mobile broadband communications. The superabundant spectrum available at these mmWave bands is capable to deliver high data rates and capacity required for future broadband cellular systems. The 5G standard is being designed to achieve latencies lower than 1 ms, with data rates up to 10 Gbps, high network reliability, and higher positioning accuracy. However, transmissions at mmWave bands suffer more from higher pathloss and susceptibility to blockage than lower band signals [1]. To compensate for a larger pathloss and provide efficient communication, 5G networks utilizing mmWave frequencies require both a transmitter (Tx) and a receiver (Rx) to form narrow beams using a large number of antenna arrays [2,3].

Because location awareness is a fundamental feature of many new markets such as emergency services [4] and location-aware communications [5], positioning is considered an integral part of upcoming 5G New Radio (5G NR) systems [6]. Currently, the mobile station (MS) position is acquired from the Global Navigation Satellite Systems (GNSS), which has worldwide coverage and perform sufficiently in a perfectly clear sky. However, satellite perceptibility is constrained in urban canyons and indoors. Thus, a substitutive approach is to use the cellular infrastructure itself with localization techniques such as trilateration or fingerprinting [7]. In the current LTE standard [8,9], specific positioning methods such as positioning reference signal (PRS), long-term evolution (LTE) positioning protocol (LPP), and PRS muting along with the network resources are used. Moreover, indoor positioning enhancement was studied in the standardization process [10] to achieve a horizontal position precision of 50 m for E911 emergency services [4]. Meanwhile, as the predecessor of future 5G networks, there is a growing demand in the use of positioning with high-accuracy in LTE [11]. Compared with legacy cellular networks such as LTE, one of the major changes in NR is the addition of mmWave frequency bands. As part of the specification work in NR [12], the positioning solutions that will be supported include downlink time difference of arrival (DTDoA), uplink-TDoA (UTDoA), multi-cell round trip

* Corresponding author.
E-mail addresses: snhk02@gmail.com (M.S. Khan), changhwan.park.kr@gmail.com (C.H. Park), jgjoung@cau.ac.kr (J. Joung), yscho@cau.ac.kr (Y.S. Cho).

https://doi.org/10.1016/j.vehcom.2021.100358
2214-2096/© 2021 The Author(s). Published by Elsevier Inc. This is an open access article under the CC BY-NC-ND license (http://creativecommons.org/licenses/by-nc-nd/4.0/).

time (MRTT), downlink angle-of-departure (DAoD), Uplink angle-of-arrival (UAoA), and enhanced cell identity (ECID) [13].

Previously, various techniques were developed for positioning and orientation estimation for mmWave bands [14,6,15–19] and massive multiple-input multiple-output (MIMO) systems [20–25]. By measuring the received signal strength (RSS), meter-level positioning accuracy was obtained in [14], but the RSS modeling is very sensitive to the mismatch of the pathloss model of the mmWave systems. In [6,15,16], joint position and orientation estimation algorithms are proposed to show that a single base station (BS) is sufficient to use the estimated AoA/AoD for the line-of-sight (LoS) path to locate an MS. In [17], the estimation and tracking of the AoA through beam switching were considered. In this approach, it was assumed that the none-LoS (NLoS) components originate from a single bounce scatter. In [18], user positioning was formulated as a hypothesis testing problem, thereby limiting the estimation of AoA to spatial resolution. In the case of massive-MIMO, [20] proposed a direct positioning method by combining the observations of distributed massive MIMO BSs, where LoS path must be present and NLoS paths are regarded as the interference. In [21], the joint estimation of delay, AoD, and AoA was proposed and the effect of errors in phase shifters and delays were investigated, but only under LoS conditions. By using the extended Kalman filter (EKF), the combination of AoAs and observed TDoAs (OTDoAs), and the combination of AoDs and ToAs with MS tracking methods were presented in [22] and [23,24], respectively. However, the corresponding state-transition model of EKF that describes the mobility characteristics of the MS is considered as linear in [22–24], which is not an optimum choice for tracking. In [25], a tensor-based multi-dimensional channel and position estimation algorithm is proposed. It showed the improvement of channel estimation accuracy in the microwave-band with rich scattering, but it requires an alternating least-squares procedure and cannot guarantee convergence.

Among the numerous application areas of NR, one of the most important applications is vehicle-to-infrastructure (V2I), Vehicle-to-vehicle (V2V), or vehicle-to-everything (V2X) [26]. MmWave V2X communication systems are being considered due to their potential for Gbps data rates [27]. Since NR is based on orthogonal frequency division multiplexing (OFDM), mmWave V2X system is sensitive to Doppler shifts due to the swift motion in a high-frequency band and requires Doppler compensation. However, full Doppler compensation cannot be guaranteed in mmWave V2X systems and small frequency error may lead to a severe performance loss in OFDM-based mmWave V2X systems. Doppler compensation is even more challenging in OFDM-based mmWave V2X systems under a cooperative transmission mode, where adjacent high-speed vehicles (HSVs) introduce their own carrier frequency offset (CFO) contributions [28]. The Doppler shift also produces an ambiguity in timing estimation, which is used for positioning.

For positioning in mmWave V2X systems, OTDoA/UTDoA measurements used in 3G or dedicated pilot patterns (positioning reference signal; PRS) in LTE can be considered. However, these cellular generations are currently unable to meet the positioning requirements of the future vehicular networks [29]. In the OTDoA procedure, the MS searches for the signal transmitted from the neighboring BSs using correlators, from which the propagation delays can be detected to calculate the MS position using trilateration. In addition, UTDoA is very similar to OTDoA except that it uses the uplink signal, from the MS to the BSs, rather than the downlink signal. Because the signal must possess a good autocorrelation property for accurate timing estimation [30], sequences such as LTE PRS (Gold sequence) or Zadoff–Chu (ZC) sequence have been used for OTDoA and UTDoA estimations, respectively [31–34]. However, these sequences may be unsuitable for HSVs in mmWave V2X systems due to their sensitivity to Doppler. For the ZC sequence, the effect of Doppler shift was investigated, and solutions are provided in [30,34]. But, the solutions in [30,34] are not applicable in mmWave systems due to the mmWave's higher carrier frequencies and correspondingly higher Doppler shifts. Timing estimation in a high Doppler environment with conventional sequences/waveforms may lead to inaccurate position estimation. In addition, impulse radio waveform [35] and visible light communication [36] are envisioned for vehicle positioning. However, visible light communication cannot be used for the positioning of HSVs in mmWave systems. Thus, a new sequence/waveform that is robust to Doppler shift is required for accurate timing estimation for positioning HSVs in mmWave cellular systems. To the best of the authors' knowledge, there have been no attempts to resolve the problem of Doppler shift for positioning in mmWave cellular systems. This study aims to design a new sequence that provides accurate timing in high Doppler environments such as mmWave V2X communication systems.

RADAR and SONAR systems rely extensively on analog waveforms (such as pulse and linear frequency modulated (LFM)) and discrete coded waveforms (such as Barker code, pseudo-random number (PRN) code, and phase codes (binary and polyphase)) to obtain Doppler and range information of a target [32]. The pulse waveform provides correct timing in the existence of small Doppler shifts. However, for the pulse waveform, the output of the matched filter is reduced significantly when a large Doppler shift exists. In a previous work [37], we presented a random-access preamble (RAP) design technique based on the LFM waveform for HSVs under very high Doppler in mmWave cellular networks. The LFM waveform is known to be Doppler-insensitive because its matched filter output produces a high peak in the existence of a large Doppler shift [32]. However, the peak location is shifted depending on the magnitude of the Doppler shift [32,37]. Thus, the LFM waveform is not adequate for accurate timing estimation in high Doppler environments. Moreover, time-domain waveforms used in RADAR and SONAR systems are not adequate for OFDM systems because the time-domain waveforms are not compatible for multiplexing with other frequency-domain signals in the OFDM system.

In addition, unlike RADAR and SONAR systems that do not need to carry the Tx identity (ID) information in the transmitted signal, a large number of cell IDs (CIDs) need to be generated in cellular systems and associated into the waveform design so that the MS can distinguish different adjacent BSs. In [32], the correlation performance of the phase-coded sequences is shown to be sensitive to Doppler shift. Even if the MS velocity is low, the matched filters output will still deteriorate significantly compared to the outputs of the static MS. In [38], Doppler tolerant Golay complementary codes based on the Prouhet-Thue-Morse sequence were designed. The sequences perform better only in small Doppler shift intervals near zero Doppler shift. Therefore, the waveforms in [32,38] are not appropriate for sequence design with good correlation properties within a limited range (delay) of the ambiguity function regardless of the value of Doppler shift.

The major contributions in this paper are summarized as follows.

- A new sequence, an oscillatory pulse sequence (OPS), for accurate time estimation considering high Doppler shifts at mmWave frequencies is proposed.
- An ambiguity function (AF) of OPS is analyzed to observe its autocorrelation property when Doppler shift and time shift exist. It is shown that the proposed OPS creates almost no time ambiguity in the existence of a large Doppler shift, provided that parameters are selected properly.
- A cross-ambiguity function (CAF) is defined and analyzed to observe the cross-correlation property of the proposed OPS with distinct CIDs in the existence of a Doppler shift. Using

the CAF, an upper bound (UB) expression is derived to obtain the number of sequences that can be generated with the OPS.
- The performance of the proposed OPS for the positioning of HSVs in a mmWave cellular environment is evaluated via computer simulations. The performance of the proposed OPS is compared with the performance of LTE PRS, ZC, and LFM waveforms with respect to correlation, time ambiguity, and Doppler tolerance.

The rest of this paper is organized as follows. In Section 2, the system model and position estimation algorithm are described. In Section 3, the concept of the proposed OPS is described. The AF and CAF of OPS are derived to analyze correlation properties of OPS in the existence of the Doppler shift. The number of possible sequences that can be generated with the OPS is also derived. In Section 4, the performance of the proposed OPS for the positioning of HSV is evaluated using a basic model of a mmWave cellular system and compared with well-known state-of-the-art sequences. Conclusions are drawn in Section 5.

2. Preliminaries

2.1. System model

Consider an mmWave cellular system employing uniform linear arrays (ULAs) with N_{Tx} and N_{Rx} transmit and receive antenna elements, respectively. When a signal vector $\mathbf{x}^c(n) \in \mathbb{C}^{N_{Tx}\times 1}$ is transmitted simultaneously from the transmit array at the cth BS, all the signal vectors received by the receiving array at the uth HSV in the cth cell through N_L paths, $\mathbf{y}^{u,c}(n) = \left[y_1^{u,c}(n),\ y_2^{u,c}(n),\ \cdots,\ y_{N_{Rx}N_{Tx}}^{u,c}(n)\right]^{\mathrm{T}} \in \mathbb{C}^{N_{Rx}N_{Tx}\times 1}$, is given as

$$\mathbf{y}^{u,c}(n) = \sum_{l=1}^{N_L} \alpha_l^{u,c} \boldsymbol{A}_l^{u,c} x_l^c\left(n - n_l^d\right) e^{j2\pi \frac{f_D \tau n}{N_s}} + \mathbf{w}(n), \quad 0 \leqslant n < N_s \tag{1}$$

where $\boldsymbol{A}_l^{u,c} = vec\left[\mathbf{a}^u\left(\theta_l^u\right)\left(\mathbf{a}^c\left(\phi_l^c\right)\right)^{\dagger}\right]$. Here, $\mathbf{a}^u\left(\theta_l^u\right) \in \mathbb{C}^{N_{Rx}\times 1}$ is the receive array steering vector at u^{th} HSV corresponding to the AoA, $\theta_l^u \in [-\pi/2,\ \pi/2]$, of the lth path. Besides, $\mathbf{a}^c\left(\phi_l^c\right) \in \mathbb{C}^{N_{Tx}\times 1}$ is the transmit array steering vector at c^{th} BS corresponding to the AoD, $\phi_l^c \in [-\pi/2,\ \pi/2]$, of the lth path. In (1), the parameters α, n^d, f_D, τ, N_s, †, and $\mathbf{w}(n) \in \mathbb{C}^{N_{Rx}N_{Tx}\times 1}$ denote complex gain, propagation delay, Doppler shift, symbol duration, sequence length, Hermitian transform, and additive white Gaussian noise (AWGN) vector, respectively. Here, the channel is assumed to be quasi-stationary. The model in (1) is used for joint estimation of AoA and AoD [39].

Because mmWave channels have normally limited scattering [1, 40], the channel matrix $\mathbf{H}^{u,c}$ can be expressed as

$$\mathbf{H}^{u,c} = \sum_{l=1}^{N_L} \alpha_l^{u,c} \mathbf{a}^u\left(\theta_l^u\right)\left(\mathbf{a}^c\left(\phi_l^c\right)\right)^{\dagger} \tag{2}$$

When the mmWave channel has a single dominant LoS path, (2) can be rewritten as [40,41]

$$\mathbf{H}^{u,c} = \alpha^{u,c} \mathbf{a}^u\left(\theta^u\right)\left(\mathbf{a}^c\left(\phi^c\right)\right)^{\dagger} \tag{3}$$

2.2. AoA and AoD estimation

With the set of N_s samples received at each of N_{Rx} antenna elements, due to each of N_{Tx} antenna elements

$$\mathbf{Y}^{u,c} = \left[\mathbf{y}^{u,c}(0), \cdots, \mathbf{y}^{u,c}(N_s - 1)\right] \in \mathbb{C}^{N_{Rx}N_{Tx}\times N_s} \tag{4}$$

a covariance matrix is constructed as

$$\hat{\mathbf{R}}_{\mathbf{YY}} = \frac{1}{N_s}\mathbf{Y}^{u,c}\left(\mathbf{Y}^{u,c}\right)^{\dagger} \tag{5}$$

In this paper, we use 2D-MUltiple SIgnal Classification (MUSIC) algorithm to obtain AoA and AoD information although many other direction of arrival (DoA) estimation techniques are applicable. Using eigenvalue decomposition (EVD), (5) can be partitioned into signal subspace and noise subspace as follows:

$$\hat{\mathbf{R}}_{\mathbf{YY}} = \hat{\boldsymbol{V}}_s \boldsymbol{\Lambda}_s \hat{\boldsymbol{V}}_s^{\dagger} + \hat{\boldsymbol{V}}_w \boldsymbol{\Lambda}_w \hat{\boldsymbol{V}}_w^{\dagger} \tag{6}$$

where $\boldsymbol{\Lambda}_s$ is a diagonal matrix containing the largest N_L eigenvalues, $\boldsymbol{\Lambda}_w$ is a diagonal matrix with the smallest $N_{Rx}N_{Tx} - N_L$ eigenvalues, $\hat{\boldsymbol{V}}_s$ is a signal subspace composed of the eigenvectors corresponding to the largest N_L eigenvalues of $\hat{\mathbf{R}}_{\mathbf{YY}}$, and $\hat{\boldsymbol{V}}_w$ is a noise subspace composed of the remaining eigenvectors. To estimate AoA and AoD, 2D-MUSIC spatial spectrum is computed as follows [39]:

$$\Upsilon\left(\theta^u, \phi^c\right) = \frac{1}{\boldsymbol{\varphi}^{\dagger}\hat{\boldsymbol{V}}_w \hat{\boldsymbol{V}}_w^{\dagger}\boldsymbol{\varphi}} \tag{7}$$

where $\boldsymbol{\varphi} = \mathbf{a}^u\left(\theta^u\right) \otimes \mathbf{a}^c\left(\phi^c\right)$ and $\otimes$ is the Kronecker product. Finally, N_L largest peaks of $\Upsilon\left(\theta^u, \phi^c\right)$ are found to obtain AoA and AoD estimates. For a single LoS path, $\hat{\theta}^u, \hat{\phi}^c = \underset{\theta^u,\phi^c}{\arg\max}\, \Upsilon\left(\theta^u, \phi^c\right)$. Note that any other subspace-based algorithm can be used instead of 2D-MUSIC to reduce the computational cost.

2.3. Distance estimation

After forming Tx and Rx beams at the BS and HSV using the estimated AoD and AoA, respectively, the HSV receives the signal, $\bar{\mathbf{y}}^{u,c} = vec\left[\mathbf{a}^u\left(\hat{\theta}^u\right)\left(\mathbf{a}^c\left(\hat{\phi}^c\right)\right)^{\dagger}\right]^{\dagger}\mathbf{Y}^{u,c} \in \mathbb{C}^{1\times N_s}$. The correlation between the received signal and a locally generated reference sequence is performed to estimate the propagation delay. After estimating the propagation delay, the distance between BS, c, and HSV, u, is estimated as

$$\hat{D} = \frac{v \cdot \hat{n}^d \tau}{N_s} = \frac{v \cdot \hat{n}^d}{\Delta f N_s} \tag{8}$$

where v is the propagation velocity of the signal (i.e., light speed) and Δf is the subcarrier spacing. Finally, the position $[\chi^u, \gamma^u]$ of the HSV is obtained using the estimated distance, AoA, and AoD information as follows:

$$\hat{\chi}^u = \hat{D}\sin\hat{\theta}^u,\ \hat{\gamma}^u = \hat{D}\cos\hat{\theta}^u \tag{9}$$

3. Proposed oscillatory pulse sequence (OPS)

3.1. Concept

The AF is an analytic tool for waveform design and analysis, which can compactly characterize the behavior of waveforms paired with matched filters. Moreover, it is useful to examine the resolution, sidelobe behavior, and ambiguities in both Doppler and delay (time shift) of a given waveform. Fig. 1 shows the time-domain waveforms (such as pulse in Fig. 1a and LFM in Fig. 1b) and their corresponding AF contours that are widely used in RADAR and SONAR systems. At zero Doppler shift, the AF of a pulse waveform with duration τ follows a triangular function, oriented along the delay axis (Fig. 1d). Similarly, the AF of a pulse waveform follows a sinc function along the Doppler axis at zero

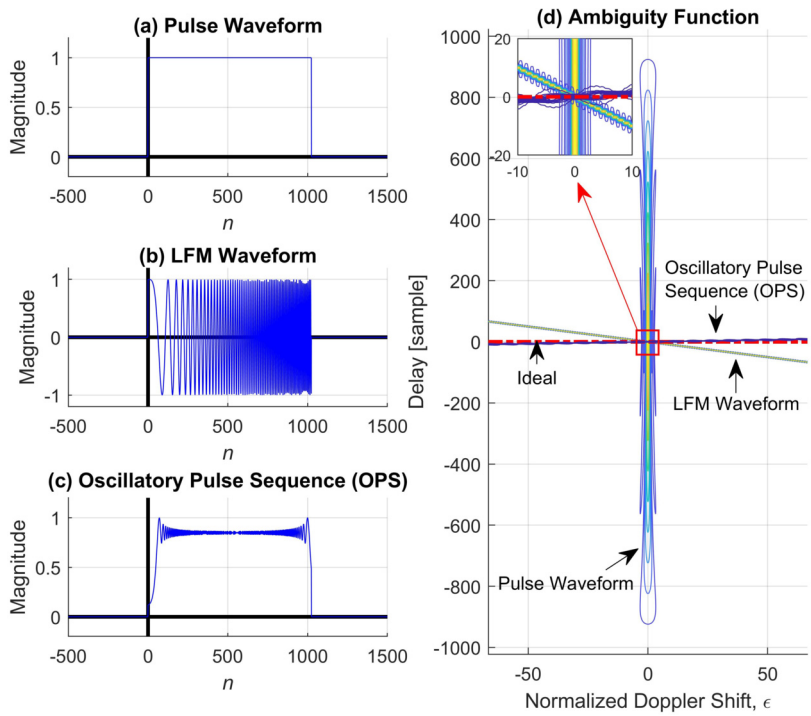

Fig. 1. (a) Pulse, (b) LFM, (c) OPS, and (d) Ambiguity functions of Pulse, LFM ($\beta^c = 15.36$ MHz), and OPS ($q = 0.1302$) with bandwidth $B = \Delta f N_s$, when $\Delta f = 15$ kHz and $N_s = 1024$.

delay and becomes zero at a Doppler mismatch of $\pm 1/\tau$ Hz. Thus, the peak of the pulse waveform's AF remains at the correct timing when the Doppler mismatch is small ($< 1/\tau$). For the LFM waveform, in turn, duration, τ, and swept bandwidth, β^c, can be used independently to control the pulse energy and delay resolution. The AF of LFM holds the triangular ridge of the pulse waveform but is now skewed in the delay-Doppler plane (Fig. 1d). AF of LFM is the same (sinc function) as that of the pulse waveform along the Doppler axis at zero delay. However, when there is a Doppler mismatch, its peak will not occur at the correct time and will shift in proportion to the value of Doppler shift.

The LFM waveforms are extensively used for monitoring/surveillance applications because the target needs to be detected under the influence of high Doppler. However, the LFM waveform is not adequate for positioning in high Doppler environments because it cannot produce the correct timing. Note that an ideal AF changes with the application. The AF of LFM waveform (a skewed version of the triangular ridge in the delay-Doppler plane) is beneficial for surveillance applications. In contrast, for positioning in high Doppler environments, a waveform will be beneficial if its AF can produce high peaks at the correct timing regardless of the amount of the Doppler shift. Thus, the ideal AF will be "a line" located on the horizontal (Doppler shift) axis. To the best of the authors' knowledge, waveform with the characteristic ("a line" on the Doppler axis) of the ideal AF have not been found so far. In this study, we develop a new sequence, called an OPS (Fig. 1c), which possesses the characteristic of the ideal AF shown in Fig. 1d. In Fig. 1d, the Doppler shift is normalized by Δf such that the normalized Doppler shift, $\varepsilon = f_D/\Delta f$, and the parameter q used to generate OPS in Fig. 1c is explained in the next subsection.

3.2. Generation and properties of OPS

Although the OPS is generated in the frequency domain and mapped to the subcarriers in the OFDM system, we start with the time-domain description because of its familiarity. A time-domain LFM waveform for CID c is given in (10) [32].

$$x^c_{LFM}(t) = e^{j\pi \frac{\beta^c}{\tau} t^2}, \quad 0 \leqslant t < \tau \tag{10}$$

where τ is symbol duration, $-B \leqslant \beta^c \leqslant B$ is the frequency sweeping parameter and B is the channel bandwidth. Note that the frequency sweeping parameter β^c is distinct for each cell (CID c). The proposed OPS is generated by sampling the LFM waveform and mapping the samples to subcarriers in the frequency-domain resource grid. Let $T = \tau/N_s$ be the sampling interval and N_s be the number of samples, then the corresponding sampled signal of (10) is given by (11).

$$x^c_{LFM}(n) = \begin{cases} e^{\frac{j\pi}{N_s}\beta^c T n^2}, & 0 \leqslant n \leqslant N_s - 1 \\ 0, & \text{elsewhere} \end{cases} \tag{11}$$

After mapping the sampled signal to N_s subcarriers of the OFDM symbol in the frequency resource grid, the signal in frequency-domain is transformed into a time-domain signal via an N-point IDFT. With the assumption that N is equal to N_s, the N_s-point IDFT of the signal given in (11) can be given as

$$\begin{aligned} \tilde{x}^c(n) &= \frac{1}{N_s} \sum_{k=0}^{N_s-1} e^{\frac{j\pi}{N_s} q k^2} e^{\frac{j2\pi nk}{N_s}} \\ &= \frac{1}{N_s} \sum_{k=0}^{N_s-1} e^{\frac{j\pi}{N_s} q \left[(k+nq^{-1})^2 - (nq^{-1})^2 \right]} \end{aligned} \tag{12}$$

where $q = \beta^c T$. Since, k can be treated as a quasi-continuous variable, the sum over all integral values of k can be approximately replaced by an integral [42] as (13).

$$\tilde{x}^c(n) \approx \frac{1}{N_s} e^{-\frac{j\pi}{qN_s} n^2} \int_0^{N_s-1} e^{\frac{j\pi}{N_s} q (k+nq^{-1})^2} dk \tag{13}$$

Substituting $\eta = k + nq^{-1}$ in (13),

$$\tilde{x}^c(n) \approx \frac{1}{N_s} e^{-\frac{j\pi}{qN_s}n^2} \int_{nq^{-1}}^{N_s+nq^{-1}-1} e^{\frac{j\pi}{N_s}q\eta^2} d\eta \tag{14}$$

Substituting $\eta\sqrt{j\pi q/N_s} = \mu$ and $d\eta = \sqrt{N_s/j\pi q}\,d\mu$ in (14),

$$\begin{aligned}\tilde{x}^c(n) &\approx \frac{1}{N_s} e^{-\frac{j\pi}{qN_s}n^2} \int_{n\sqrt{\frac{j\pi}{qN_s}}}^{(N_s+nq^{-1}-1)\sqrt{\frac{j\pi q}{N_s}}} e^{\mu^2}\sqrt{\frac{N_s}{j\pi q}}\,d\mu \\ &\approx \frac{1}{2\sqrt{jqN_s}} e^{-\frac{j\pi}{qN_s}n^2} \\ &\quad \left[erfi\left(\left(N_s+\frac{n}{q}-1\right)\sqrt{\frac{j\pi q}{N_s}}\right) - erfi\left(n\sqrt{\frac{j\pi}{qN_s}}\right)\right]\end{aligned} \tag{15}$$

The relationship between *erfi* and Fresnel integral is given as [43]

$$\begin{aligned}erfi(z) &= \frac{2}{\sqrt{\pi}}\int_0^z e^{\mu^2}dt \\ &= (1-j)\left(C\left(\frac{(1+j)z}{\sqrt{\pi}}\right) - jS\left(\frac{(1+j)z}{\sqrt{\pi}}\right)\right)\end{aligned} \tag{16}$$

Substituting (16) in (15),

$$\begin{aligned}\tilde{x}^c(n) &\approx \frac{1}{2\sqrt{jqN_s}} e^{-\frac{j\pi}{qN_s}n^2}(1-j) \\ &\quad \begin{bmatrix} C\left(\frac{(1+j)z_1}{\sqrt{\pi}}\right) - jS\left(\frac{(1+j)z_1}{\sqrt{\pi}}\right) \\ -C\left(\frac{(1+j)z_2}{\sqrt{\pi}}\right) + jS\left(\frac{(1+j)z_2}{\sqrt{\pi}}\right)\end{bmatrix} \\ &\approx \frac{1}{2\sqrt{jqN_s}} e^{-\frac{j\pi}{qN_s}n^2}(1-j) \\ &\quad \left[Z\left(\frac{(1+j)z_1}{\sqrt{\pi}}\right) - Z\left(\frac{(1+j)z_2}{\sqrt{\pi}}\right)\right]\end{aligned} \tag{17}$$

In (17), $z_1 = \left(N_s + \frac{n}{q} - 1\right)\sqrt{\frac{j\pi q}{N_s}}$, and $z_2 = n\sqrt{\frac{j\pi}{qN_s}}$. Additionally, $erfi$, C, S, and Z denote the imaginary error function, cosine Fresnel integral, sine Fresnel integral, and complex conjugate Fresnel integral, respectively [44]. Fig. 2 shows the generation process of the OPS.

(17) can be divided into two terms: a phase term and a Fresnel amplitude term. The Fresnel term is similar to a rectangular function and the phase term is similar to the LFM waveform given in (11). Thus, the proposed OPS can be approximated as an LFM waveform where the parameter q is in the denominator of the phase term instead of numerator as that of the LFM waveform. This significantly increases the time-bandwidth ($B\tau$) product of the OPS, resulting in the increase of pulse compression, for the same value of q in the LFM waveform and OPS. It follows that the OPS AF cut along delay axis is narrower than that of the unmodulated pulse by a factor of N_s/q or $N_s^2/\beta^c\tau$. Note that the performance (target detection and range resolution) of a waveform increases as its $B\tau$ product increases. For instance, when $q = 0.0326$ (i.e., $\beta^c = 0.5$ MHz with $T = 65.10$ ns), the LFM waveform will be generated with the value of $q = 0.0326$. In the OPS with the same value of q, the effective value of the parameter is $1/q$, which is 942.4 times higher than q. Thus, the OPS produces significantly lower time shift than the LFM waveform and provides accurate timing in the existence of a large Doppler shift. In addition, the bandwidth of the OPS remains constant regardless of the value of β^c. The bandwidth of OPS is given by the multiplication

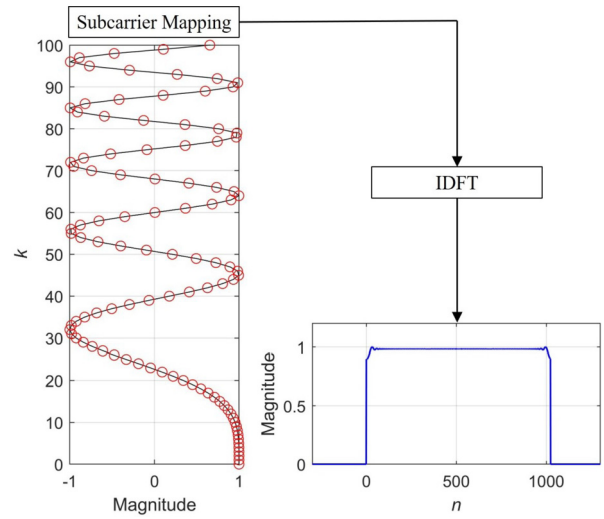

Fig. 2. Generation of the OPS ($q = 0.9961$).

of subcarrier spacing and the number of subcarriers (i.e., $\Delta f N_s$) used for OPS generation in OFDM systems.

In order to examine the autocorrelation property of OPS in the existence of Doppler, the AF of OPS in the discrete-time domain is given as

$$R^c(m,\varepsilon) = \sum_{s=0}^{N_s-1} \tilde{x}^c(s)\tilde{x}^c(s-m)^* e^{\frac{j2\pi\varepsilon s}{N_s}} \tag{18}$$

Substituting (12) into (18), the AF can be derived as shown in (19).

$$\begin{aligned}R^c(m,\varepsilon) &= \frac{1}{N_s^2}\sum_{s=0}^{N_s-1} e^{-\frac{j\pi}{qN_s}\left(s^2-(s-m)^2\right)} e^{\frac{j2\pi\varepsilon s}{N_s}} \sum_{d=0}^{N_s-1} \\ &\quad \times \sum_{g=0}^{N_s-1} e^{\frac{j\pi q}{N_s}\left(d+\frac{s}{q}\right)^2} e^{\frac{-j\pi q}{N_s}\left(g+\frac{(s-m)}{q}\right)^2} \\ &= \frac{1}{N_s^2} e^{\frac{j\pi m^2}{qN_s}} \sum_{d=0}^{N_s-1}\sum_{g=0}^{N_s-1} e^{\frac{j\pi q d^2}{N_s}} e^{\frac{-j\pi q}{N_s}\left(g-\frac{m}{q}\right)^2} \sum_{s=0}^{N_s-1} e^{\frac{j2\pi}{N_s}(\varepsilon+d-g)s} \\ &= \frac{1}{N_s^2} e^{\frac{j\pi m^2}{qN_s}} \sum_{d=0}^{N_s-1}\sum_{g=0}^{N_s-1} e^{\frac{j\pi q d^2}{N_s}} e^{\frac{-j\pi q}{N_s}\left(g-\frac{m}{q}\right)^2} \frac{1-e^{j2\pi(\varepsilon+d-g)}}{1-e^{\frac{j2\pi}{N_s}(\varepsilon+d-g)}} \\ &= \frac{1}{N_s^2} e^{\frac{j\pi m^2}{qN_s}} \begin{cases} \sum_{d=0}^{N_s+m-1}\sum_{g=0}^{N_s+m-1} e^{\frac{j\pi q}{N_s}\left(d^2-g^2+\frac{2mg}{q^2}\right)} e^{j\pi\frac{(N_s-1)(\varepsilon+d-g)}{N_s}} \\ \quad \times \frac{\sin(\pi(\varepsilon+d-g))}{\sin\left(\frac{\pi}{N_s}(\varepsilon+d-g)\right)}, & -N_s < m \leqslant 0 \\ \sum_{d=0}^{N_s-m-1}\sum_{g=0}^{N_s-m-1} e^{\frac{j\pi q}{N_s}\left(d^2-g^2+\frac{2mg}{q^2}\right)} e^{j\pi\frac{(N_s-1)(\varepsilon+d-g)}{N_s}} \\ \quad \times \frac{\sin(\pi(\varepsilon+d-g))}{\sin\left(\frac{\pi}{N_s}(\varepsilon+d-g)\right)}, & 0 < m < N_s \end{cases}\end{aligned} \tag{19}$$

In (19), $\varepsilon = f_D\tau$ with f_D being the Doppler shift and $d, g \in [0, N_s-1]$. As can be seen from (19), the magnitude of AF of OPS varies with the values of q and ε. In addition, the magnitude is one at the origin ($m = 0, \varepsilon = 0$). When $d = g$ and $m = 0$, (19) is approximated as (20) which is only true for $q = 1$ (i.e., $\beta^c = B$).

$$R^c(0,\varepsilon) \approx e^{j\pi\frac{(N_s-1)\varepsilon}{N_s}} \frac{\mathrm{sinc}(\pi\varepsilon)}{\mathrm{sinc}\left(\frac{\pi\varepsilon}{N_s}\right)} \tag{20}$$

Assuming $\varepsilon \ll N_s$, the AF magnitude in (20) at zero timing error can further be approximated as $\left|R^c(0,\varepsilon)\right| \approx |\mathrm{sinc}(\varepsilon)|$, which is a sinc function of ε.

Further, to find the cross-correlation property of the proposed OPS with distinct CIDs (c, c') in the existence of Doppler, the CAF of two OPSs with q and q' is defined and derived as (21).

$$\begin{aligned} R^{c,c'}(m,\varepsilon) &= \sum_{s=0}^{N_s-1} \tilde{x}^c(s)\,\tilde{x}^{c'}(s-m)^* e^{\frac{j2\pi\varepsilon s}{N_s}} \\ &= \frac{1}{N_s^2} e^{\frac{j\pi m^2}{q' N_s}} \sum_{d=0}^{N_s-1}\sum_{g=0}^{N_s-1} e^{\frac{j\pi q d^2}{N_s}} e^{-\frac{j\pi q'}{N_s}\left(g-\frac{m}{q'}\right)^2} \frac{1-e^{j2\pi(\varepsilon+d-g)}}{1-e^{\frac{j2\pi}{N_s}(\varepsilon+d-g)}} \\ &= \frac{1}{N_s^2} e^{\frac{j\pi m^2}{q' N_s}} \begin{cases} \sum_{d=0}^{N_s+m-1}\sum_{g=0}^{N_s+m-1} e^{\frac{j\pi q d^2}{N_s}} e^{-\frac{j\pi q'}{N_s}\left(g-\frac{m}{q'}\right)^2} e^{j\pi\frac{(N_s-1)(\varepsilon+d-g)}{N_s}} \\ \quad \times \frac{\sin(\pi(\varepsilon+d-g))}{\sin\left(\frac{\pi}{N_s}(\varepsilon+d-g)\right)}, & -N_s < m \leqslant 0 \\ \sum_{d=0}^{N_s-m-1}\sum_{g=0}^{N_s-m-1} e^{\frac{j\pi q d^2}{N_s}} e^{-\frac{j\pi q'}{N_s}\left(g-\frac{m}{q'}\right)^2} e^{j\pi\frac{(N_s-1)(\varepsilon+d-g)}{N_s}} \\ \quad \times \frac{\sin(\pi(\varepsilon+d-g))}{\sin\left(\frac{\pi}{N_s}(\varepsilon+d-g)\right)}, & 0 < m < N_s \end{cases} \end{aligned} \tag{21}$$

In (21), $q' = \beta^{c'} T$. When $d = g$, (21) can be approximated by Fresnel integrals as (22).

$$\begin{aligned} R^{c,c'}(m,\varepsilon) &\approx \frac{1}{N_s^2} e^{j\pi\frac{(N_s-1)\varepsilon}{N_s}} \frac{\sin(\pi\varepsilon)}{\sin(\pi\varepsilon/N_s)} \sum_{d=0}^{N_s-1} e^{j\pi\left(\frac{2m}{N_s}d+\frac{\Delta q}{N_s}d^2\right)} \\ &\approx \frac{\sin(\pi\varepsilon)}{N_s^2\sin(\pi\varepsilon/N_s)} e^{\frac{j\pi}{N_s}\left[(N_s-1)\varepsilon-\frac{(mN_s)^2}{\Delta q}\right]} \left(\frac{C^{c,c'}(m)}{N_s a^{c,c'}} + j\,\mathrm{sgn}(\Delta q)\frac{S^{c,c'}(m)}{N_s a^{c,c'}}\right) \end{aligned} \tag{22}$$

where $\mathrm{sgn}(\cdot)$ is the signum function, $\Delta q = q - q'$, $\Delta q \neq 0$, and

$$\begin{aligned} C^{c,c'}(m) &= C\left(a^{c,c'}s_0 + b^{c,c'}(m)\right) + C\left(a^{c,c'}s_m - b^{c,c'}(m)\right), \\ S^{c,c'}(m) &= S\left(a^{c,c'}s_0 + b^{c,c'}(m)\right) + S\left(a^{c,c'}s_m - b^{c,c'}(m)\right), \\ s_m &= \frac{N_s}{2} - |m|,\ a^{c,c'} = \sqrt{\frac{\Delta q\pi}{N_s}}, b^{c,c'}(m) = \frac{m}{\Delta q}\sqrt{\pi\Delta q N_s} \end{aligned} \tag{23}$$

In addition, the time shift, $\bar{m}^c$, can be derived as follows:

$$\bar{m}^c = q\varepsilon = \frac{\beta^c\tau\varepsilon}{N_s} = \frac{\beta^c\tau^2 f_D}{N_s} \tag{24}$$

In (24), the time shift is linearly approximated. It can be seen that for given values of τ and N_s, the time shift increases with β^c and f_D.

The separation Δq between the two OPSs with q and q' must be cautiously selected to have a low correlation between them while supporting a large number of sequences. The number of sequences that can be generated with the OPS is obtained using an UB of the CAF. To provide the UB of the CAF, the following relationships are obtained:

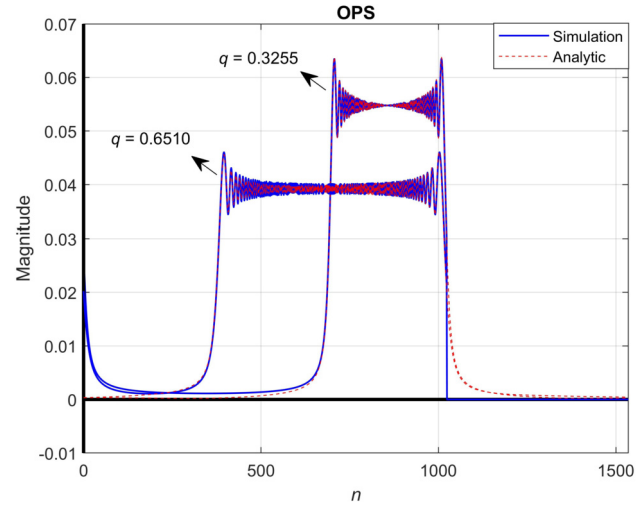

Fig. 3. Comparison between simulated and analytic OPS in the time domain.

$$\begin{aligned} &-C_{\max} \leqslant C(m) \leqslant C_{\max},\ -S_{\max} \leqslant S(m) \leqslant S_{\max}, \\ &-2C_{\max} \leqslant C(m_1) + C(m_2) \leqslant 2C_{\max}, \\ &-2S_{\max} \leqslant S(m_1) + S(m_2) \leqslant 2S_{\max}, \\ &0 \leqslant \left[C^{c,c'}(m)\right]^2 \leqslant 4C_{\max}^2,\ 0 \leqslant \left[S^{c,c'}(m)\right]^2 \leqslant 4S_{\max}^2, \\ &0 \leqslant \left[C^{c,c'}(m)\right]^2 + \left[S^{c,c'}(m)\right]^2 \leqslant 4\left(C_{\max}^2 + S_{\max}^2\right), \\ &0 \leqslant \frac{\left[C^{c,c'}(m)\right]^2 + \left[S^{c,c'}(m)\right]^2}{\left(N_s a^{c,c'}\right)^2} \leqslant \frac{4\left(C_{\max}^2 + S_{\max}^2\right)}{\left(N_s a^{c,c'}\right)^2}, \\ &0 \leqslant \left|R^{c,c'}(m,\varepsilon)\right| \leqslant \frac{2}{N_s a^{c,c'}}\sqrt{C_{\max}^2 + S_{\max}^2} \end{aligned} \tag{25}$$

Now, the UB of the CAF can be derived using the relationships in (25) as follows:

$$\xi(\Delta q) = 2\sqrt{\frac{C_{\max}^2 + S_{\max}^2}{\pi\Delta q N_s}} \tag{26}$$

where $C_{\max} = 0.9775$ and $S_{\max} = 0.8948$ denote the non-normalized maximum cosine and sine Fresnel integrals [44], respectively. In (26), the values of UB are robust to the selection of Doppler shift f_D, indicating that f_D have no significant effect on the CAF magnitude. However, the symbol duration ($\tau = TN_s$) and Δq are vital. The larger the $\Delta q N_s$, the smaller the UB. Using (26), the number of sequences that can be generated with the OPS is obtained as follows:

$$\Gamma(\Delta q) = 2\left(\frac{1-q^0}{\Delta q} + 1\right) \tag{27}$$

where q^0 (i.e., $\beta^0 T$) denotes the minimum value of q. In (27), the larger the value of Δq, the smaller the number of sequences that can be generated with the OPS. In (27), the value of Δq can be determined using the UB of the CAF in (26) as follows:

$$\Delta q = 4\frac{C_{\max}^2 + S_{\max}^2}{\pi N_s \xi(\Delta q)} \tag{28}$$

In (28), the value of Δq increases as the values of N_s or UB of CAF $\xi(\Delta q)$ decreases. From (26) and (28), a value of Δq must be selected appropriately such that it can provide low cross-correlation levels for large number of sequences.

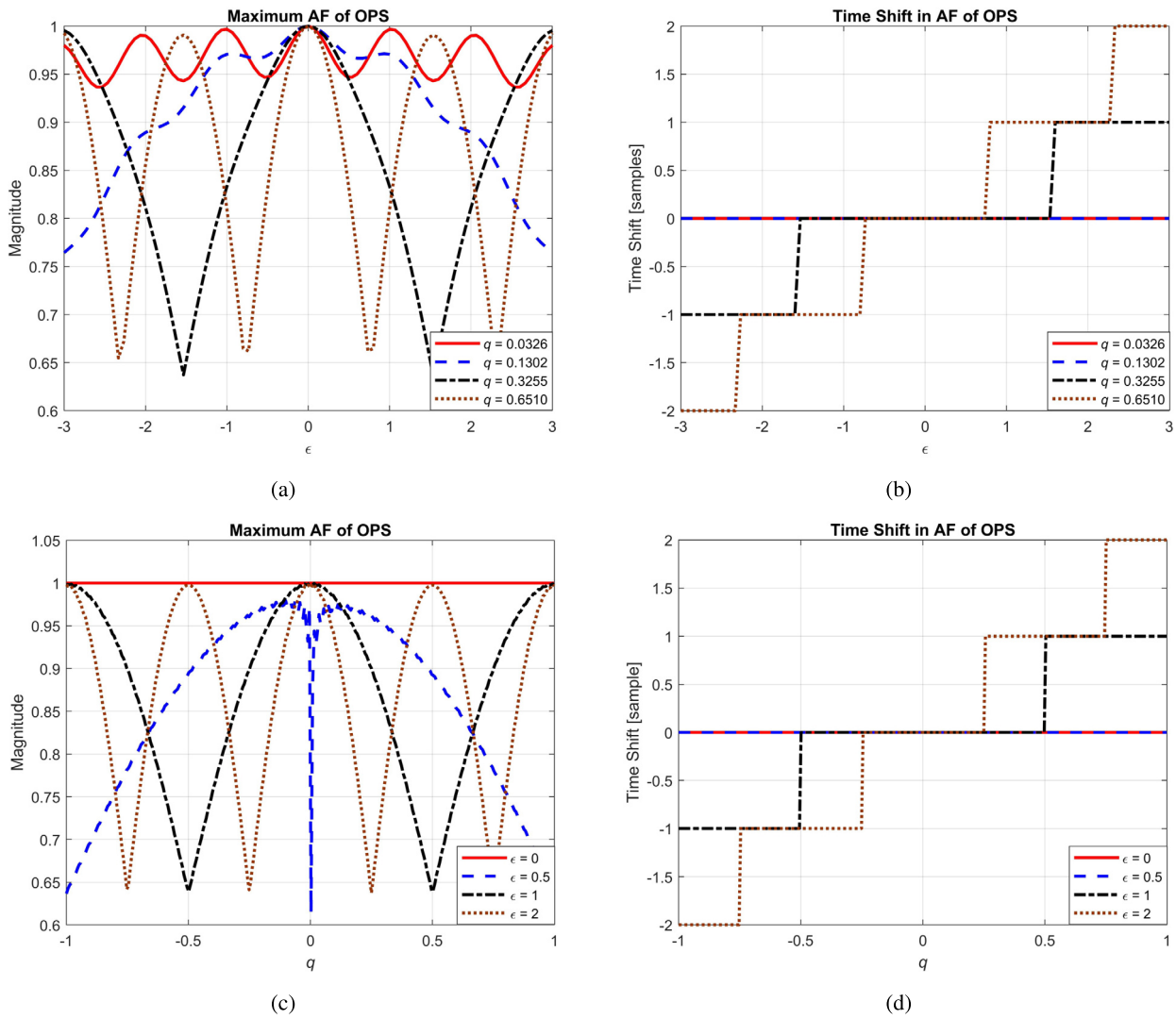

Fig. 4. Maximum magnitude and corresponding time shift in AF of OPS: (a) maximum magnitude vs. ε, (b) time shift vs. ε, (c) maximum magnitude vs. q, (d) time shift vs. q.

4. Simulation

In this section, the basic model of the mmWave cellular system is used to evaluate the performance of the proposed OPS along with the conventional sequences (such as LTE PRS, ZC, and LFM) for the positioning of HSV through computer simulation. Unless otherwise mentioned, the subcarrier spacing (Δf), carrier frequency (f_c), and length of the sequence (N_s) are 15 kHz, 28 GHz, and 1024, respectively. The beamforming antenna configuration used at both BS and HSV is a ULA with eight antenna elements. For performance evaluation, the scenarios are set to estimate the position of the HSV in outdoor environments and the spatial channel model (SCM) is used to generate multipath channels. In the simulation, a Rician fading channel consisting of a line-of-sight (LoS) path and non-line-of-sight (NLoS) path is used. The k-factor is set to 10 dB and the number of rays in the NLoS path is set to 20. The rays in the NLoS path have the mean AoD/AoA randomly selected from the values of $[-90^\circ\ 89^\circ]$ and an azimuth spread of 2°.

In Fig. 1d, the time-domain LFM and OPS waveforms are generated with the values of β^c and q as 15.36 MHz and 0.1302, respectively. From Fig. 1, it can be seen that the AF of OPS with the aforementioned parameters appears closer to the ideal AF (a "line") located on the Doppler shift axis. Thus, one can see that the OPS provides accurate timing in the existence of a large Doppler shift. The following figures show the detailed AF characteristics of the OPS when the parameters vary.

First, the properties of OPS discussed in Section 3 are verified considering $\Delta f = 15$ kHz. Fig. 3 compares the analytic solution obtained in (17) with the simulation results. As $q = \beta^c T$, the value of q is altered by altering β^c while T is constant. In this figure, two OPSs with $q \in \{0.3255, 0.6510\}$ corresponding to $\beta^c \in \{5, 10\}$ MHz are shown, respectively. The figure shows that the simulation results agree well with the analytic solution given in (17).

Fig. 4 shows the maximum magnitude and corresponding time shift in AF of OPS with varying ε and q. Fig. 4a and Fig. 4b show the simulation results evaluated over ε domain for $q \in \{0.0326, 0.1302, 0.3255, 0.6510\}$ corresponding to $\beta^c \in \{0.5, 2, 5, 10\}$ MHz, respectively. Fig. 4c and Fig. 4d show the results evaluated over q domain for $\varepsilon \in \{0, 0.5, 1, 2\}$ respectively. From these figures, it can be seen that when $\varepsilon = 0$, the maximum magnitude is one for all q and no time shift occurs. However, the maximum magnitude changes with the existence of Doppler shift, and the corresponding time shift occurs. Fig. 4a and Fig. 4b show that when q is 0.0326, the maximum magnitude never goes below 93% and no time shift occurs. When q increases, the magnitude decreases following the sinc function and the corresponding time shift occurs. For instance, when $q \in \{0.3255,\ 0.6510\}$, the time shift of one sample occurs at $\varepsilon \in \{\pm 1.5,\ \pm 0.75\}$. Fig. 4c and Fig. 4d

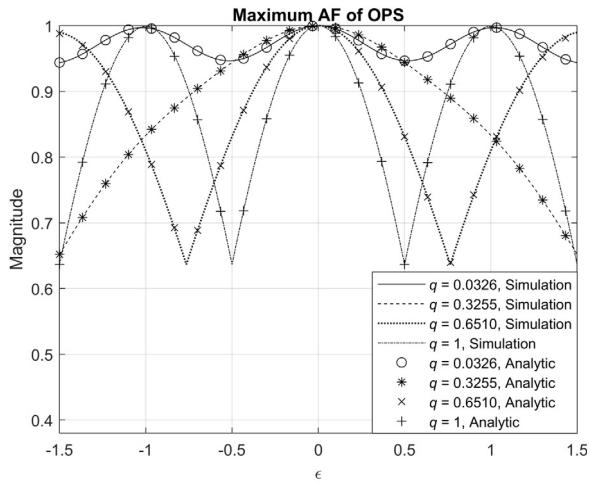

(a)

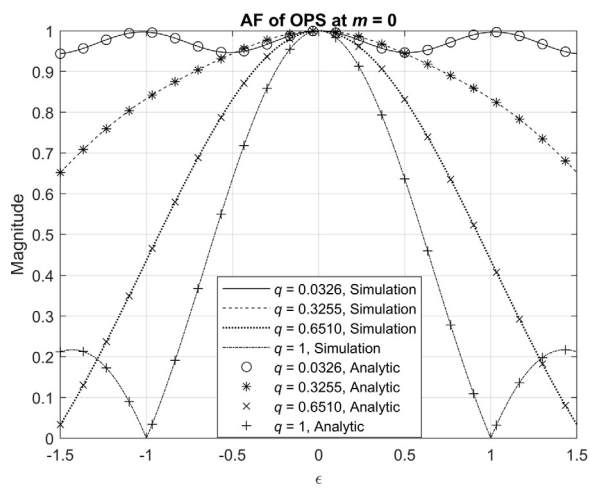

(b)

Fig. 5. AF of OPS with varying ε: (a) maximum magnitude, (b) magnitude at $m = 0$.

show that when the Doppler shift exists, the maximum magnitude decreases faster for larger values of q and the corresponding time shift occurs. For instance, when $\varepsilon \in \{1,\ 2\}$, the side peak with equal magnitude occurs at $q \in \{\pm 0.5052,\ \pm 0.2513\}$ and the time shift of one sample occurs for the values of $q \geqslant \{\pm 0.5052,\ \pm 0.2513\}$.

Fig. 5 shows the comparative simulation and analytic results for AF of OPS with varying ε as given in (19) and (20). Fig. 5a and Fig. 5b show the maximum magnitude and magnitude at $m = 0$ of AF of OPS in the ε domain with $q \in \{0.0326, 0.3255, 0.6510, 1\}$, respectively. From Fig. 4 and Fig. 5, it can be seen that the smaller values of q are more robust to the Doppler shift and as the value of q increases, the sensitivity to Doppler increases. Fig. 5 indicates that the analytic results given in (19) and (20) agrees with the simulation results for all values of ε and q.

Fig. 6 shows the comparative simulation and analytic results for CAF of OPS, as given in (21) and (22). Fig. 6a and Fig. 6b show the maximum magnitude and magnitude at $m = 0$ of CAF of two OPSs in the ε domain with $q = 0.0326$ and $q' \in \{0.1302, 0.3255, 0.6510, 1\}$, respectively. Fig. 6c shows the cross-correlation of two OPSs in time-domain for $\varepsilon = 0$ when $q = 0.0326$ and $q' \in \{0.1302,\ 0.3255\}$. As can be seen from these figures, the increase in Δq decreases the magnitude of CAF. This signifies that the value of cross-correlation of two distinct OPSs becomes smaller with the increase in the value of Δq. These results suggest that the

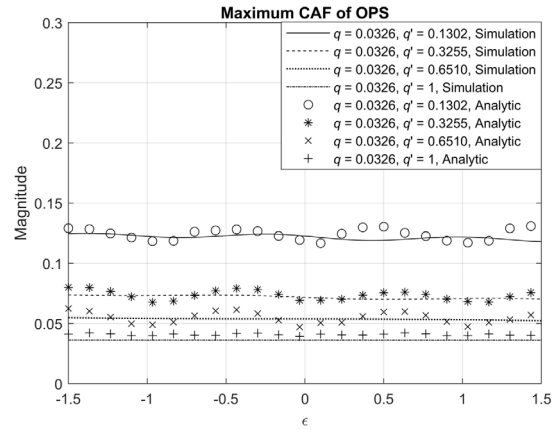

(a)

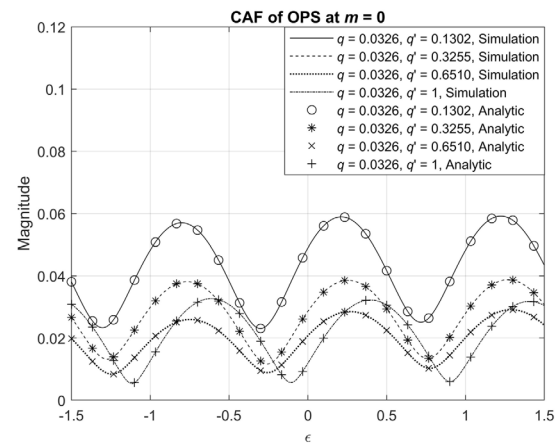

(b)

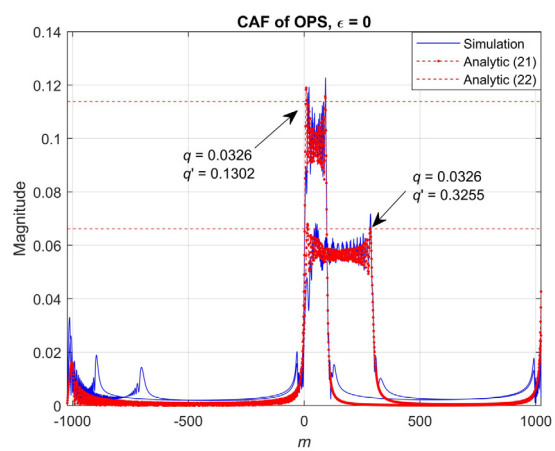

(c)

Fig. 6. CAF of OPS: (a) maximum magnitude vs. ε, (b) magnitude at $m = 0$ vs. ε, (c) magnitude at $\varepsilon = 0$ vs. m.

analytic solution obtained in (21) and (22) agrees with the simulation results.

Fig. 7 compares the maximum CAF of OPS from the simulation with the analytic UB given in (26). To obtain Fig. 7, the value of q is set to q^0 as 0.0326 and $\tau \in \{66.67, 33.35, 16.67\}\mu s$ corresponding to $\Delta f \in \{15,\ 30,\ 60\}$ kHz. In addition, the value of q' is determined by changing Δq. In Fig. 7, UB decreases with the in-

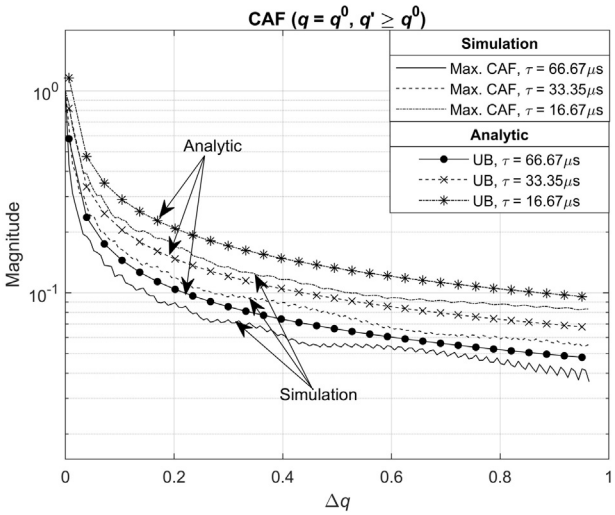

Fig. 7. Upper bound and maximum CAF of OPS.

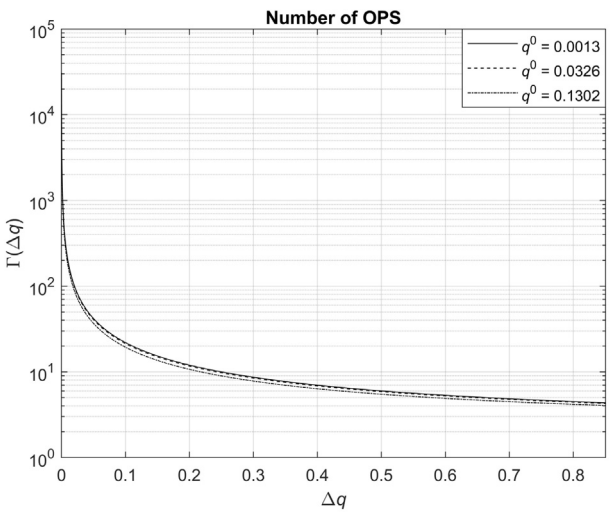

Fig. 8. Number of possible OPSs with different q^0.

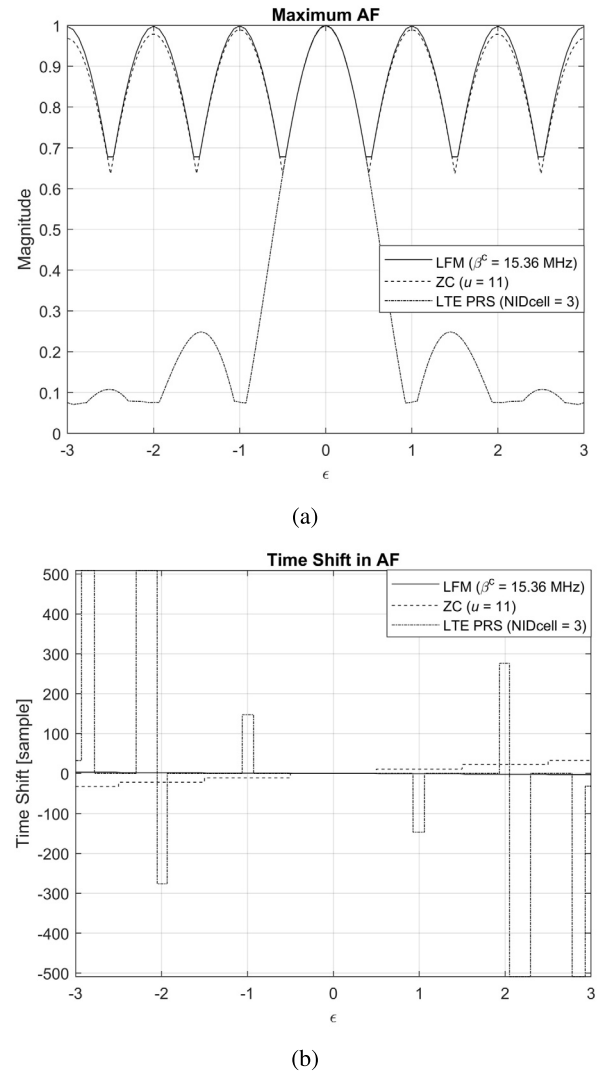

Fig. 9. Maximum magnitude and corresponding time shift in AF of LFM, ZC and LTE PRS: (a) maximum magnitude vs. ε (b) time shift vs. ε.

crease of Δq and τ. The analytic UBs are slightly higher than the simulation results.

Fig. 8 shows the number of possible sequences that can be generated by the OPS. This figure is obtained from (27) by changing Δq for $q^0 \in \{0.0013, 0.0326, 0.1302\}$. In Fig. 8, the number of sequences is inversely proportional to Δq and also depends on the value of q^0. For instance, when the values of Δq are 0.0043, 0.026, 0.03, and 0.13, the number of OPSs that can be generated are 453, 77, 67, and 17, respectively. Therefore, it can be concluded that in the sequence design with the OPS, there is a trade-off with the selection of Δq between the magnitude of cross-correlation level and the possible number of sequences.

Similar to Fig. 4, Fig. 9 shows the maximum magnitude and corresponding time shift in AF of sequences such as LFM ($\beta^c = 15.36$ MHz), ZC (*root index*, $u = 11$), and LTE PRS (*NIDcell* $= 3$) [8], with varying ε. Note that the PRS is used to determine the location of HSV and the ZC sequence is used for preamble design (primary synchronization signals), all in LTE systems. In Fig. 9, it is shown that when $\varepsilon = 0$, the maximum magnitude is one, and no time shift occurs regardless of the sequence used. However, the maximum magnitude fluctuates in the existence of Doppler shift and the corresponding time shift occurs, for all the sequences. For instance, when $\varepsilon \in \pm\{0.5, 1, 2\}$, the time shift of {1, 1, 2} samples, {11, 11, 22} samples, and {0, 147, 276} occurs for LFM, ZC, and LTE PRS, respectively. Whereas, for $\varepsilon \in \pm\{0.5, 1, 2\}$, the time shift of {0, 0, 0} sample (i.e., no time shift) occurs for OPS $q = 0.1302$ as shown in Fig. 4.

In Fig. 10, the positioning error using LTE PRS, ZC, LFM ($\beta^c = \Delta f N_s$), and OPS ($q = 0.1302$) is shown. Here, a single BS and HSV located at the origin ([0, 0]) and [100 m, 50 m] are considered, respectively. Adopting the system model in Section 2, the positioning error in terms of normalized mean square error (NMSE) is evaluated when $\Delta f \in \{15, 60\}$ kHz and $f_D \in \{0, 15\}$ kHz. As can be seen from Fig. 10a when $f_D = 0$ kHz, the positioning error is the same regardless of the sequence transmitted at the higher values of SNR. In addition, when Δf is increased while keeping N_s constant, the sampling interval is decreased, thereby making the time delay resolution finer. The raw resolution, defined as the distance that radio waves can travel between the sampling instants, is the smallest distance difference that can be measured. Thus, the positioning error is reduced as Δf increases. At higher SNR regions, for instance -5 dB, the NMSE is reduced by 22 dB when $\Delta f = 60$ kHz is used instead of 15 kHz. Further, when $f_D = 15$ kHz (i.e., $\varepsilon = 1$) for $\Delta f = 15$ kHz, the performance of all the sequences except OPS is degraded as shown in Fig. 10b. For instance, at the SNR of -5 dB, the NMSEs of LTE PRS, ZC, LFM, and OPS are 29.4, 5.9, -17.9, and -26.5 dB, respectively, confirming that the proposed OPS is robust to Doppler in terms of timing estimation.

Table 1
Property comparison of LTE PRS, ZC, LFM, and OPS.

Property	LTE PRS	ZC	LFM	OPS
Sensitivity to Doppler	More insensitive as Δf increases (Moderate)	More insensitive as Δf increases (High)	Insensitive (Low)	Insensitive (Low)
Time shift due to Doppler	Large	Large	Small	Very small
Characteristic to Doppler	Random	Lesser as root index decreases	Lesser as β^c increases	Lesser as q decreases
Cross-correlation	Good	Good	Better as $\Delta\beta$ increases	Lesser as Δq increases
Number of IDs	Equivalent to the Cell ID	Equivalent to sequence Length N_s	One	Larger as Δq decreases
Complexity	$(2N_s-1)N_s^2$	$(2N_s-1)N_s^2$	$(2N_s-1)N_s$	$(2N_s-1)N_s^3$
Multiplexing in OFDM system	Possible	Possible	Not possible	Possible

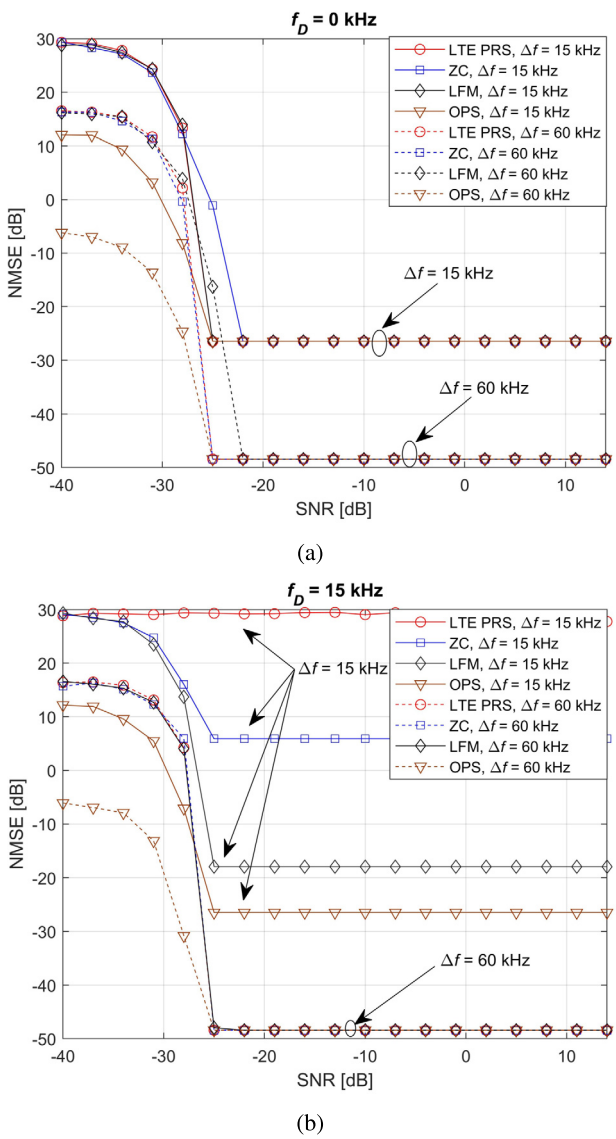

Fig. 10. Positioning error with $\Delta f = \{15, 60\}$ kHz when (a) $f_D = 0$ kHz and (b) $f_D = 15$ kHz.

Further, the system model in Section 2 is adopted to show the positioning results as shown in Fig. 11 and Fig. 12 for two scenarios where a BS (black dot) is located at the origin ([0, 0]) and an HSV is moving vertically upward in a straight path and zigzag path, respectively. Simulation results are obtained for the cases when $f_D \in \{0,\ 15\}$ kHz and when different sequences such as LTE PRS, ZC, LFM, and OPS are used as the transmitted signal with $\Delta f \in \{15,\ 30,\ 60\}$ kHz at SNR of -5 dB. In Fig. 11 and Fig. 12, a and b show the cases when $f_D = 0$ kHz and $f_D = 15$ kHz, respectively. Fig. 11a shows that the performance of position estimation is almost identical regardless of the sequence when there is no Doppler shift. Similar results are obtained for the zigzag scenario in Fig. 12a. However, when the Doppler shift exists, positioning results with (i) LTE PRS, (ii) ZC, and (iii) LFM are not correct because of the incorrectly estimated distances (Fig. 11b and Fig. 12b). Note that the distance is incorrectly estimated because of the time shift when waveforms other than OPS are used in the existence of Doppler shift. However, when the OPS is used, no time shift occurs, resulting in correct distance estimation. The positioning results obtained with (iv) OPS are presented in Fig. 11b and Fig. 12b.

Fig. 13 compares the peak-to-average power ratio (PAPR) performance of LTE PRS, ZC, LFM, and OPS. In Fig. 13a, complementary cumulative distribution functions (CCDFs) are shown for LTE PRS, ZC, LFM, and OPS. According to this figure, the PAPRs of ZC and LFM are 0 dB because they have constant envelopes. Moreover, it can be seen that the LTE PRS provides the worst PAPR performance because of the IDFT operation. The CCDF of OPS with $q = 0.9961$ is almost the same as those of ZC and LFM (i.e., PAPR $= 0$ dB). However, as the value of q decreases, the oscillation in OPS increases, resulting in the increase of PAPR as shown in Fig. 13b. In summary, the performance (Doppler insensitivity and time shifts) of OPS improves at the expense of PAPR. Finally, the properties of LTE PRS, ZC, LFM, and OPS are compared in Table 1 when they are used for delay (or position) estimation.

5. Conclusion

In this paper, a new sequence (OPS) for precise positioning of HSV in mmWave cellular systems is proposed. The OPS is shown to produce high peaks at the correct timing in the existence of Doppler shift, which is the ideal characteristic of AF for positioning. The AF and CAF of OPS, derived to examine its autocorrelation and cross-correlation properties under the existence of Doppler shift, are shown to be well-matched with the results obtained through simulation. In addition, the UB of CAF and the number of possible OPSs are analyzed for the selection of the parameters in the design of the positioning sequence. It is shown that there is a trade-off with the selection of Δq between the magnitude of cross-correlation level and the possible number of sequences generated by OPS. It is also confirmed through simulation that the OPS is suitable for positioning of HSV in mmWave cellular systems because of almost no time ambiguity in the existence of a large Doppler shift, whereas conventional waveforms such as LTE PRS, ZC, and LFM are shown to produce a large error in distance estimation. Unlike the LFM waveform, the OPS is especially suitable for OFDM systems because it can be easily multiplexed with other signals in the frequency domain. Although the proposed sequence is applied to the positioning of HSV in a mmWave cellular system in this paper, it can be applied to any communication system which requires accurate timing, distance, or position in high Doppler environments.

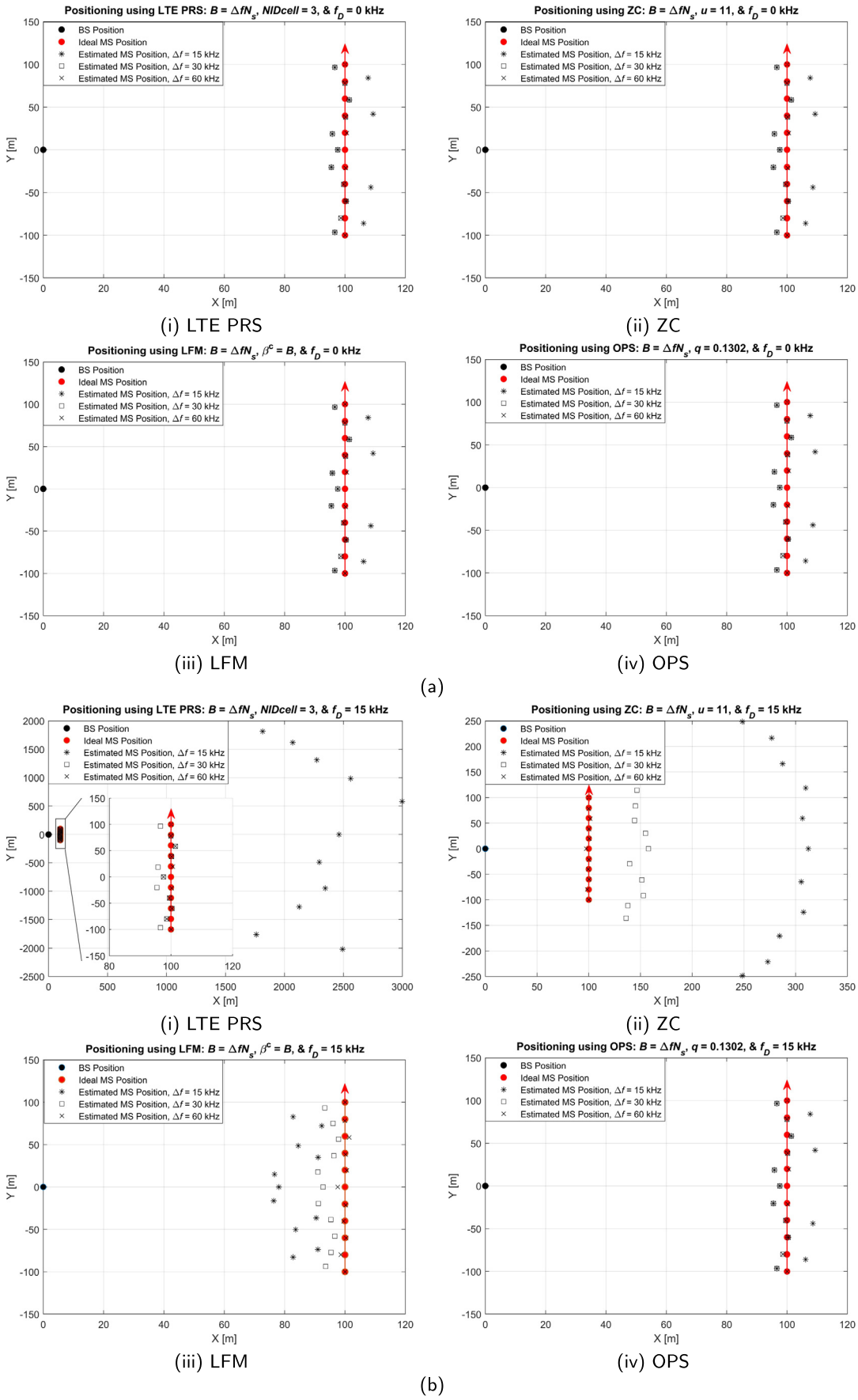

Fig. 11. Position estimation for a straight path with different Δf: (a) $f_D = 0$ kHz and (b) $f_D = 15$ kHz.

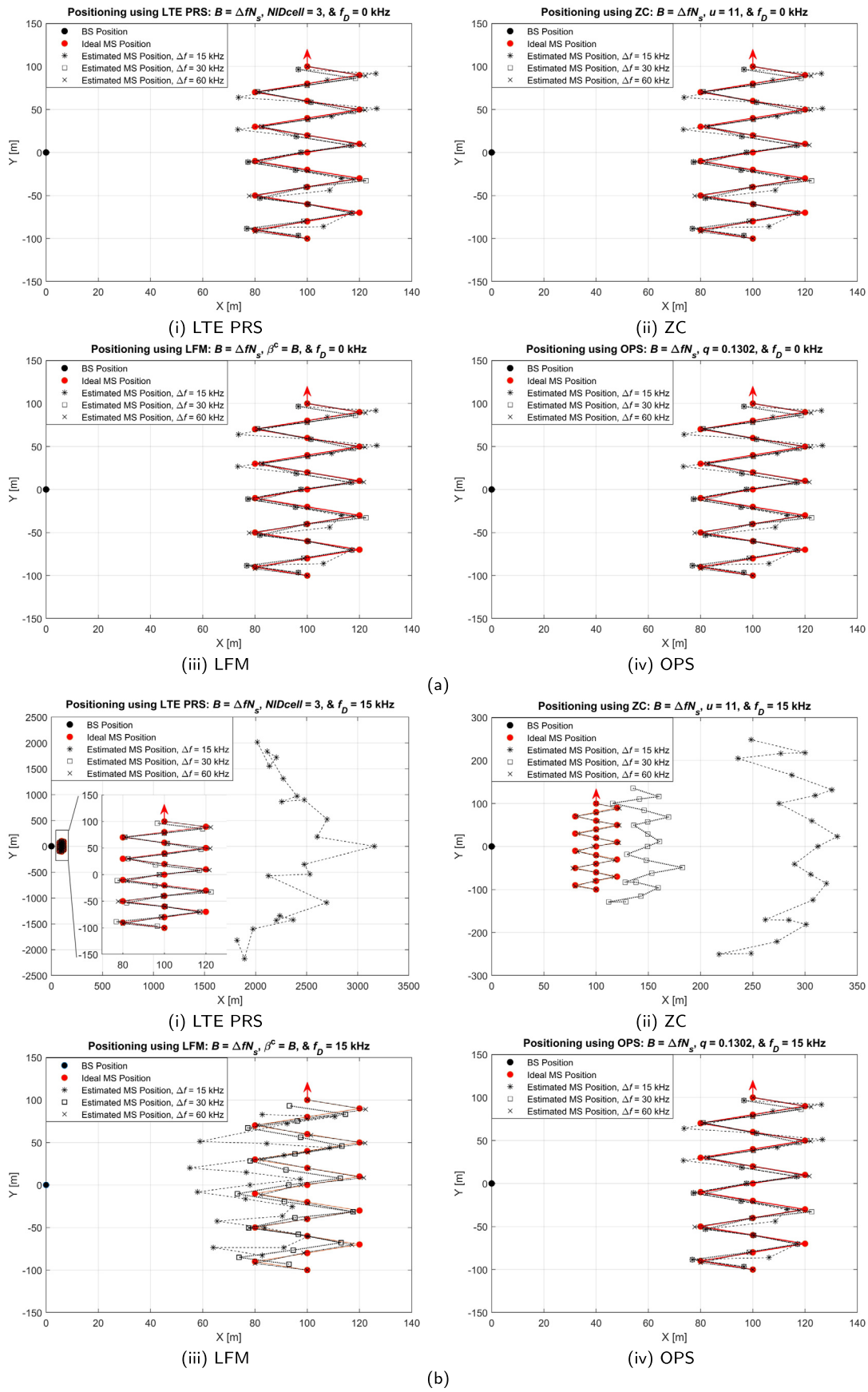

Fig. 12. Position estimation for a zigzag path with different Δf (a) $f_D = 0$ kHz and (b) $f_D = 15$ kHz.

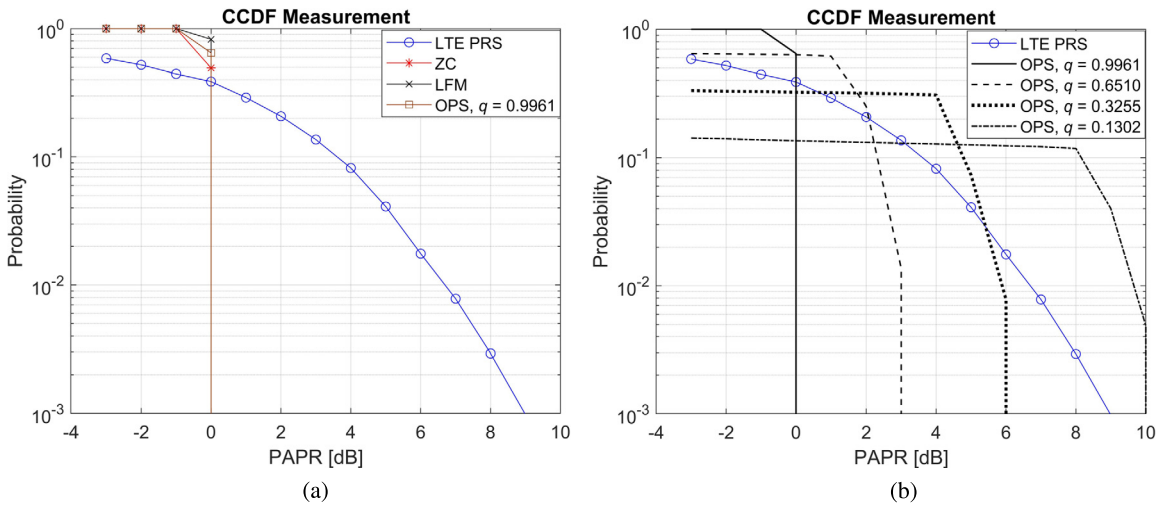

Fig. 13. PAPR performance of (a) LTE PRS, ZC, LFM, and OPS and (b) OPS with different values of q.

Declaration of competing interest

The authors declare that they have no known competing financial interests or personal relationships that could have appeared to influence the work reported in this paper.

Acknowledgement

This research was supported by the National Research Foundation of Korea (NRF) grant funded by the Korea government (MSIT) (2021R1A4A2001316) and (2018R1A2B2002621).

References

[1] T.S. Rappaport, et al., Millimeter wave mobile communications for 5G cellular: it will work!, IEEE Access 1 (2013) 335–349.
[2] M. Xiao, et al., Millimeter wave communications for future mobile networks, IEEE J. Sel. Areas Commun. 35 (2017) 1909–1935.
[3] Y. Liu, X. Fang, M. Xiao, S. Mumtaz, Decentralized beam pair selection in multi-beam millimeter-wave networks, IEEE Trans. Commun. 66 (2018) 2722–2737.
[4] Fed. Commun. Commiss., Fourth report and order on wireless E911 location accuracy requirements, Technical Report FCC 15-9, Washington, DC, USA, 2015.
[5] R.D. Taranto, et al., Location-aware communications for 5G networks: how location information can improve scalability, latency, and robustness of 5G, IEEE Signal Process. Mag. 31 (2014) 102–112.
[6] J. Talvitie, M. Valkama, G. Destino, H. Wymeersch, Novel algorithms for high-accuracy joint position and orientation estimation in 5G mmWave systems, in: 2017 IEEE Globecom Workshops, 2017, pp. 1–7.
[7] H. Liu, H. Darabi, P. Banerjee, J. Liu, Survey of wireless indoor positioning techniques and systems, IEEE Trans. Syst. Man Cybern., Part C 37 (2007) 1067–1080.
[8] LTE; Evolved Universal Terrestrial Radio Access (E-UTRA); Physical channels and modulation, 2017.
[9] LTE; Evolved Universal Terrestrial Radio Access Network (E-UTRAN); Stage 2 functional specification of user equipment (UE) positioning in E-UTRAN, 2016.
[10] Technical specification group radio access network; Study on indoor positioning enhancements for UTRA and LTE, Technical Report 37.857, 3GPP, 2015.
[11] Intel Corp., Study on LTE vehicular positioning technologies, RAN Meeting #75, 3GPP TSG RP-170427, Dubrovnik, Croatia, 2017.
[12] Technical specification group radio access network; Study on NR positioning support, Technical Report 38.855, 3GPP, 2019.
[13] Intel Corp., New WID: NR Positioning Support, RAN Meeting #83, 3GPP TSG RP-190752, Shenzhen, China, 2019.
[14] Z. Lin, T. Lv, P.T. Mathiopoulos, 3-D indoor positioning for millimeter-wave massive MIMO systems, IEEE Trans. Commun. 66 (2018) 2472–2486.
[15] A. Shahmansoori, G.E. Garcia, G. Destino, G. Seco-Granados, H. Wymeersch, Position and orientation estimation through millimeter-wave MIMO in 5G systems, IEEE Trans. Wirel. Commun. 17 (2018) 1822–1835.
[16] J. Talvitie, M. Koivisto, T. Levanen, M. Valkama, G. Destino, H. Wymeersch, High-accuracy joint position and orientation estimation in sparse 5G mmWave channel, in: 2019 IEEE International Conference on Communications, ICC, Shanghai, China, 2019, pp. 1–7.
[17] P. Sanchis, et al., A novel simultaneous tracking and direction of arrival estimation algorithm for beam-switched base station antennas in millimeter-wave wireless broadband access networks, in: IEEE Antennas and Propagation Society International Symposium, IEEE Cat. No. 02CH37313, San Antonio, TX, USA, vol. 1, 2002, pp. 594–597.
[18] H. Deng, A. Sayeed, Mm-wave MIMO channel modeling and user localization using sparse beamspace signatures, in: 2014 IEEE 15th International Workshop on Signal Processing Advances in Wireless Communications, SPAWC, Toronto, ON, Canada, 2014, pp. 130–134.
[19] H. Kim, K. Granström, L. Gao, G. Battistelli, S. Kim, H. Wymeersch, 5G mmWave cooperative positioning and mapping using multi-model PHD filter and map fusion, IEEE Trans. Wirel. Commun. 19 (2020) 3782–3795.
[20] N. Garcia, H. Wymeersch, E.G. Larsson, A.M. Haimovich, M. Coulon, Direct localization for massive MIMO, IEEE Trans. Signal Process. 65 (2017) 2475–2487.
[21] A. Guerra, F. Guidi, D. Dardari, Position and orientation error bound for wideband massive antenna arrays, in: 2015 IEEE International Conference on Communication Workshop, ICCW, London, UK, 2015, pp. 853–858.
[22] M. Koivisto, et al., High-efficiency device positioning and location-aware communications in dense 5G networks, IEEE Commun. Mag. 55 (2017) 188–195.
[23] J. Talvitie, T. Levanen, M. Koivisto, K. Pajukoski, M. Renfors, M. Valkama, Positioning of high-speed trains using 5G new radio synchronization signals, in: 2018 IEEE Wireless Communications and Networking Conference, WCNC, Barcelona, Spain, 2018, pp. 1–6.
[24] J. Talvitie, T. Levanen, M. Koivisto, K. Pajukoski, M. Renfors, M. Valkama, Positioning of high-speed trains using 5G new radio synchronization signals, arXiv:1805.01830, 2018.
[25] Z. Lin, T. Lv, J.A. Zhang, R.P. Liu, Tensor-based high-accuracy position estimation for 5G mmWave massive MIMO systems, in: 2020 IEEE International Conference on Communications, ICC, Dublin, Ireland, 2020, pp. 1–6.
[26] M. Muhammad, G.A. Safdar, Survey on existing authentication issues for cellular-assisted V2X communication, Veh. Commun. 12 (2018) 50–65.
[27] K. Lee, J. Kim, Y. Park, H. Wang, D. Hong, Latency of cellular-based V2X: perspectives on TTI-proportional latency and TTI-independent latency, IEEE Access 5 (2017) 15800–15809.
[28] X. Li, F. Ng, T. Han, Carrier frequency offset mitigation in asynchronous cooperative OFDM transmissions, IEEE Trans. Signal Process. 56 (2008) 675–685.
[29] H. Wymeersch, G. Seco-Granados, G. Destino, D. Dardari, F. Tufvesson, 5G mmWave positioning for vehicular networks, IEEE Wirel. Commun. 24 (2017) 80–86.
[30] F. Khan, LTE for 4G Mobile Broadband: Air Interface Technologies and Performance, Cambridge Univ. Press, Cambridge, UK, 2009.
[31] Z. Hans-Jurgen, A. Finger, Pseudo Random Signal Processing: Theory and Application, Wiley, Chichester, UK, 2005.
[32] B.R. Mahafza, Radar Systems Analysis and Design Using MATLAB, CRC Press, FL, USA, 2013.
[33] Y.J. Kim, D.G. Han, Y.S. Cho, A preamble sequence design technique for efficient beam ID detection in millimeter-wave cellular systems, IEEE Trans. Veh. Technol. 65 (2016) 10106–10111.
[34] X. Liu, D. Qiao, Location-fair beamforming for high speed railway communication systems, IEEE Access 6 (2018) 28632–28642.
[35] X. Cui, J. Li, Study on the impulse radio mmWave for 5G-based vehicle position, in: Wireless Algorithms, Systems, and Applications, Cham, 2017, pp. 115–123.
[36] B. Zhou, et al., Performance limits of visible light-based positioning for Internet-of-vehicles: time-domain localization cooperation gain, IEEE Trans. Intell. Transp. Syst. (2020) 1–15.

[37] M.S. Khan, R. Pec, C.H. Park, Y.S. Cho, Random access preamble design for high-velocity user in millimeter-wave cellular networks, IEEE Access 6 (2018) 66047–66054.
[38] A. Pezeshki, A.R. Calderbank, W. Moran, S.D. Howard, Doppler resilient Golay complementary waveforms, IEEE Trans. Inf. Theory 54 (2008) 4254–4266.
[39] X. Zhang, L. Xu, L. Xu, D. Xu, Direction of departure (DOD) and direction of arrival (DOA) estimation in MIMO radar with reduced-dimension MUSIC, IEEE Commun. Lett. 14 (2010) 1161–1163.
[40] M.S. Khan, S.J. Maeng, Y.S. Cho, Cell selection technique for millimeter-wave cellular systems with hybrid beamforming, Sensors 17 (2017) 1461.
[41] R.W. Heath, N. González-Prelcic, S. Rangan, W. Roh, A.M. Sayeed, An overview of signal processing techniques for millimeter wave MIMO systems, IEEE J. Sel. Top. Signal Process. 10 (2016) 436–453.
[42] F. Reif, Fundamentals of Statistical and Thermal Physics, Waveland Press, USA, 2009.
[43] Wolfram Research, Introductions to erfi, http://functions.wolfram.com/PDF/Erfi.pdf, 2020.
[44] I.S. Gradshteyn, I.M. Ryzhik, Table of Integrals, Series, and Products, Elsevier, Amsterdam, the Netherlands, 2007.